

# Structure and Formation Mechanisms in Tantalum and Niobium Oxides in Superconducting Quantum Circuits

Jin-Su Oh, Rahim Zaman, Akshay A. Murthy, Mustafa Bal, Francesco Crisa, Shaojiang Zhu, Carlos G. Torres-Castanedo, Cameron J. Kopas, Joshua Y. Mutus, Dapeng Jing, John Zasadzinski, Anna Grassellino, Alex Romanenko, Mark C. Hersam, Michael J. Bedzyk, Matt Kramer, Bi-Cheng Zhou, and Lin Zhou\*



Cite This: ACS Nano 2024, 18, 19732–19741



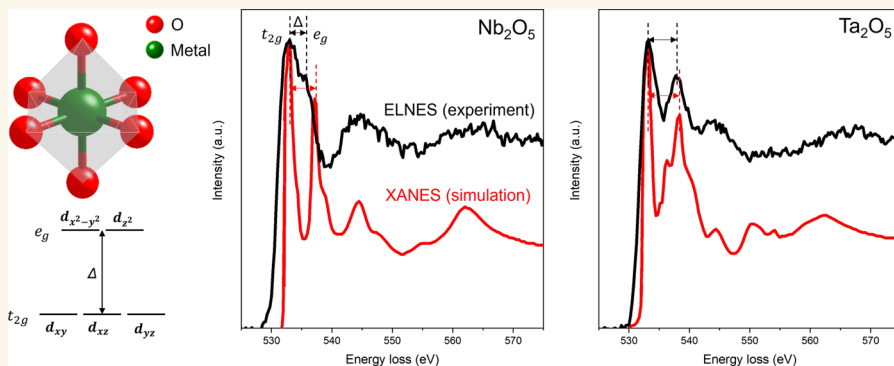
Read Online

ACCESS |

Metrics & More

Article Recommendations

Supporting Information



**ABSTRACT:** Improving the qubit's lifetime ( $T_1$ ) is crucial for fault-tolerant quantum computing. Recent advancements have shown that replacing niobium (Nb) with tantalum (Ta) as the base metal significantly increases  $T_1$ , likely due to a less lossy native surface oxide. However, understanding the formation mechanism and nature of both surface oxides is still limited. Using aberration-corrected transmission electron microscopy and electron energy loss spectroscopy, we found that Ta surface oxide has fewer suboxides than Nb oxide. We observed an abrupt oxidation state transition from  $\text{Ta}_2\text{O}_5$  to Ta, as opposed to the gradual shift from  $\text{Nb}_2\text{O}_5$ ,  $\text{NbO}_2$ , and  $\text{NbO}$  to Nb, consistent with thermodynamic modeling. Additionally, amorphous  $\text{Ta}_2\text{O}_5$  exhibits a closer-to-crystalline bonding nature than  $\text{Nb}_2\text{O}_5$ , potentially hindering H atomic diffusion toward the oxide/metal interface. Finally, we propose a loss mechanism arising from the transition between two states within the distorted octahedron in an amorphous structure, potentially causing two-level system loss. Our findings offer a deeper understanding of the differences between native amorphous Ta and Nb oxides, providing valuable insights for advancing superconducting qubits through surface oxide engineering.

**KEYWORDS:** superconducting qubits, surface encapsulation, tantalum oxides, niobium oxides, STEM-EELS, CALPHAD

Quantum information processing holds the potential to surpass traditional computers in various aspects,<sup>1,2</sup> including quantum physics, chemistry simulations,<sup>3,4</sup> and optimization algorithms.<sup>5</sup> Among the diverse materials considered for quantum computing, superconducting materials offer significant possibilities for solid-state platforms.<sup>6,7</sup> Their fabrication utilizes well-established semiconductor methodologies,<sup>8</sup> such as thin film deposition and lithography, which place a superconducting quantum bit (qubit) at the forefront of quantum computing technology.<sup>9</sup>

Over the last two decades, the advancement of superconducting qubits has primarily stemmed from optimizing the design of the quantum circuit.<sup>10–14</sup> However, it is widely

Received: April 21, 2024

Revised: July 2, 2024

Accepted: July 5, 2024

Published: July 22, 2024



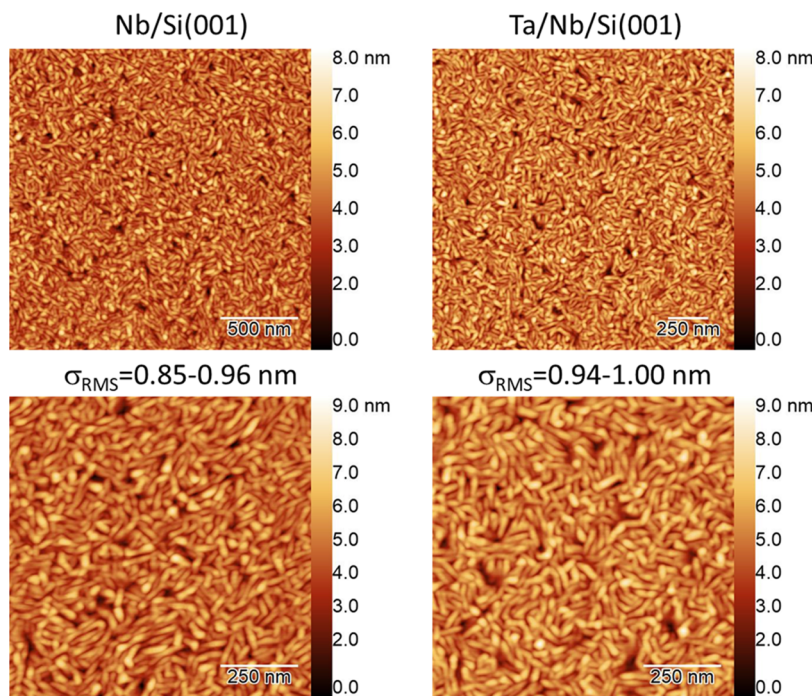


**Figure 1.** AFM surface images of Nb/Si and Ta/Nb/Si samples.

acknowledged that intricate processing methodologies can introduce defects at the interfaces and surfaces of the superconducting quantum circuits, thereby introducing decoherence sources.<sup>15–18</sup> Therefore, a precise understanding of how the material's structure and defects contribute to decoherence is essential for enhancing the performance of superconducting qubits. This understanding is particularly crucial for the Josephson junction (JJ) and resonators, which serve as fundamental components in the superconducting quantum circuits.<sup>19</sup>

Niobium (Nb)-based superconducting quantum devices have dominated the field for an extended period as this material offers cost advantages, flexibility in deposition methodologies, and compatibility with industrial-scale processes.<sup>20,21</sup> Nonetheless, as the  $T_1$  of two-dimensional transmon qubits composed of Nb has long plateaued around  $100\ \mu s$ , it has become clear that alternative materials approaches are needed.<sup>22</sup> Recent work highlights Nb surface oxides' critical role in limiting  $T_1$ .<sup>23</sup> As a result, encapsulating the surface of niobium with various metals and dielectrics allows for significant improvements, with 2–5× longer  $T_1$  achievable compared to bare Nb. Through this approach, Bal et al. achieved a maximum  $T_1$  of  $602\ \mu s$ , with a tantalum (Ta) capping layer on Nb.<sup>23</sup> This demonstrates that Ta oxide is less lossy than Nb oxide and explains why other groups have previously been able to achieve max  $T_1$  values of  $360\ \mu s$  (Place et al.,<sup>24</sup> reported Ta-based qubits) and  $503\ \mu s$  (Wang et al.,<sup>25</sup> demonstrated a further improvement through the implementation of a dry-etch process) with Ta. This improvement has been attributed to factors such as a thinner total surface oxide thickness,<sup>26</sup> a reduced number or absence of stable suboxides on the Ta surface,<sup>21,25–27</sup> or the abrupt transition from higher oxidation states to lower ones.<sup>21,26</sup> However, Bal et al.<sup>23</sup> suggest no clear correlation between oxide thickness and overall loss. Instead, they propose that this loss may arise from variations in the chemical stoichiometry (i.e., the presence of stable suboxides in the Nb oxide). Other potential factors

include variations in the local crystallinity and the presence of impurities. Despite these extensive studies, the reasons for forming fewer suboxides in Ta and their lower dissipative nature in terms of dielectric loss remain unclear. Furthermore, as niobium pentoxide is the most detrimental part of qubit's coherence,<sup>17,28,29</sup> the low-loss characteristics of tantalum pentoxide may be another reason for performance enhancement. Thus, a direct comparison between the Ta and Nb pentoxides should be carried out thoroughly.

We systematically compare microstructure and device performance fabricated from two superconducting thin films, as discussed by Bal et al.:<sup>23</sup> (1) an uncapped Nb thin film on a silicon (Si) substrate (later called the uncapped film) and (2) Ta-capped Nb thin film on Si. Our results suggest that Ta oxide is less lossy than Nb oxide due not only to the formation of less complicated oxides but also to a closer-to-crystalline nature of the oxide bonding. Our results offer valuable insights for advancing superconducting qubits through surface oxide engineering.

## RESULTS AND DISCUSSION

As discussed, Ta capping of Nb leads to a 2–5× improvement in the qubit  $T_1$ .<sup>23</sup> This enhanced  $T_1$  suggests that the notable systematic improvements are intricately linked to the metal-air (M-A) interface rather than the superconducting metal itself.<sup>23</sup> To evaluate the origin of the differences in loss between Ta and Nb oxides, we performed a detailed comparison of the M-A interface for both the Nb and Ta-capped Nb films.

Overall, the surface morphologies are nearly identical between the two samples. Figure 1 shows the atomic force microscopy (AFM) images of the Nb- and Ta-capped samples. The film's root-mean-square (RMS) roughness is less than 1 nm, exhibiting a similar value between the bare Nb and Ta-capped Nb thin films.

Cross-sectional transmission electron microscopy (TEM) micrographs in Figure 2 show that both samples exhibit

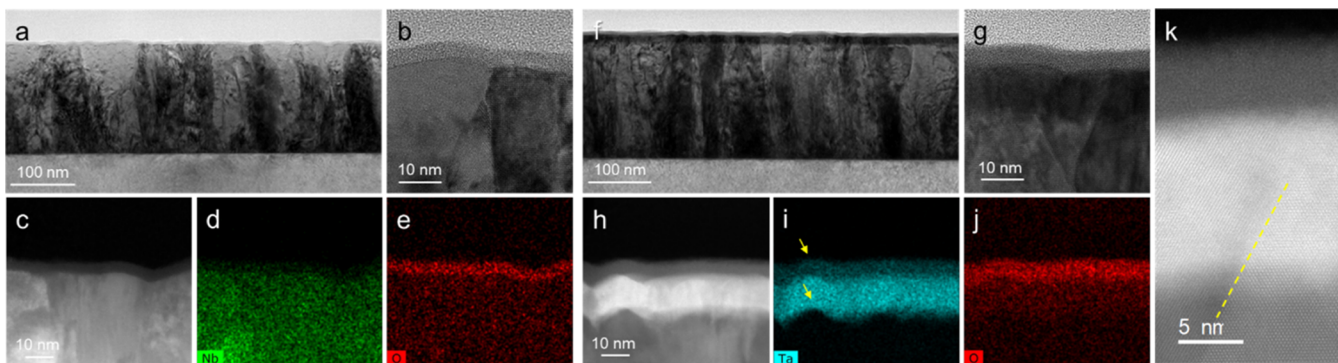


**Figure 2.** Cross-sectional TEM images of bare Nb and Ta-capped Nb thin films. **a**, Cross-sectional bright-field TEM image and **b**, high-resolution TEM image of the bare Nb thin film on Si. **c**, HAADF-STEM image and **d**, **e**, the corresponding EDS elemental distribution maps of Nb and O at the  $\text{NbO}_x\text{-Nb}$  interface. **f**, Cross-sectional bright-field TEM image and **g**, high-resolution TEM image of the Ta-capped Nb thin film on Si. **h**, HAADF-STEM image and **i**, **j**, the corresponding EDS elemental distribution map of Ta and O at the  $\text{TaO}_x\text{-Ta-Nb}$  interface. **k**, Atomic-resolution HAADF-STEM showing epitaxial growth of Ta on Nb.

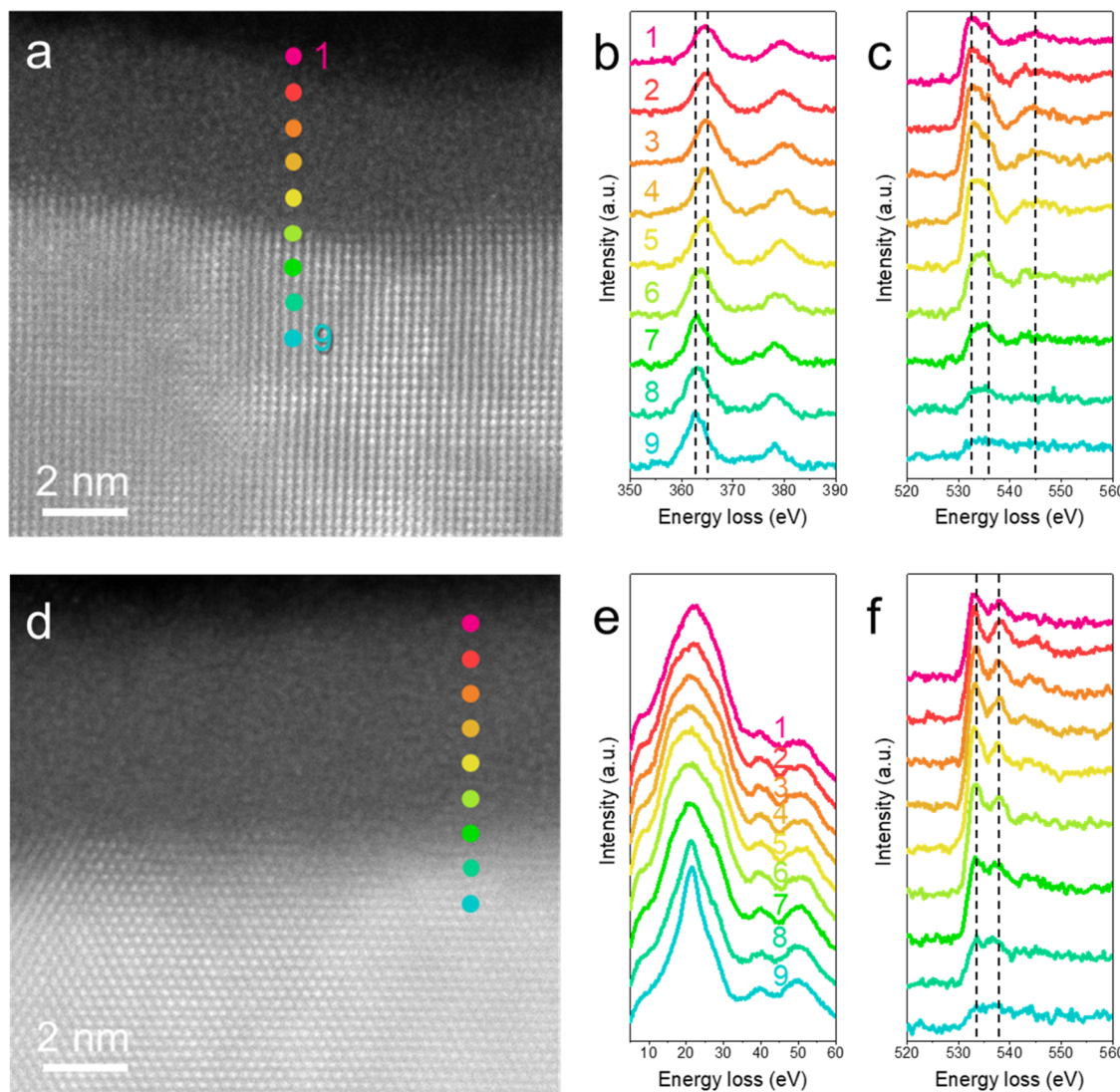


**Figure 3.** EELS line profiles of surface oxides on Nb and Ta. **a**, HAADF-STEM micrograph of the  $\text{NbO}_x\text{-Nb}$  interface of the bare Nb thin film. Colored spots denote the positions in which EEL spectra are taken. **b**, **c**, Corresponding spatially resolved EEL spectra showing ELNESs of Nb  $M_{23}$  edge and O K edge. **d**, HAADF-STEM micrograph of the  $\text{TaO}_x\text{-Ta}$  interface of Ta-capped Nb thin film. Colored spots denote the positions in which EEL spectra are acquired. **e**, **f**, Corresponding spatially resolved EEL spectra showing ELNESs of Ta  $O_{23}$  edge and O K edge. The distance between adjacent spots is 0.83 nm.

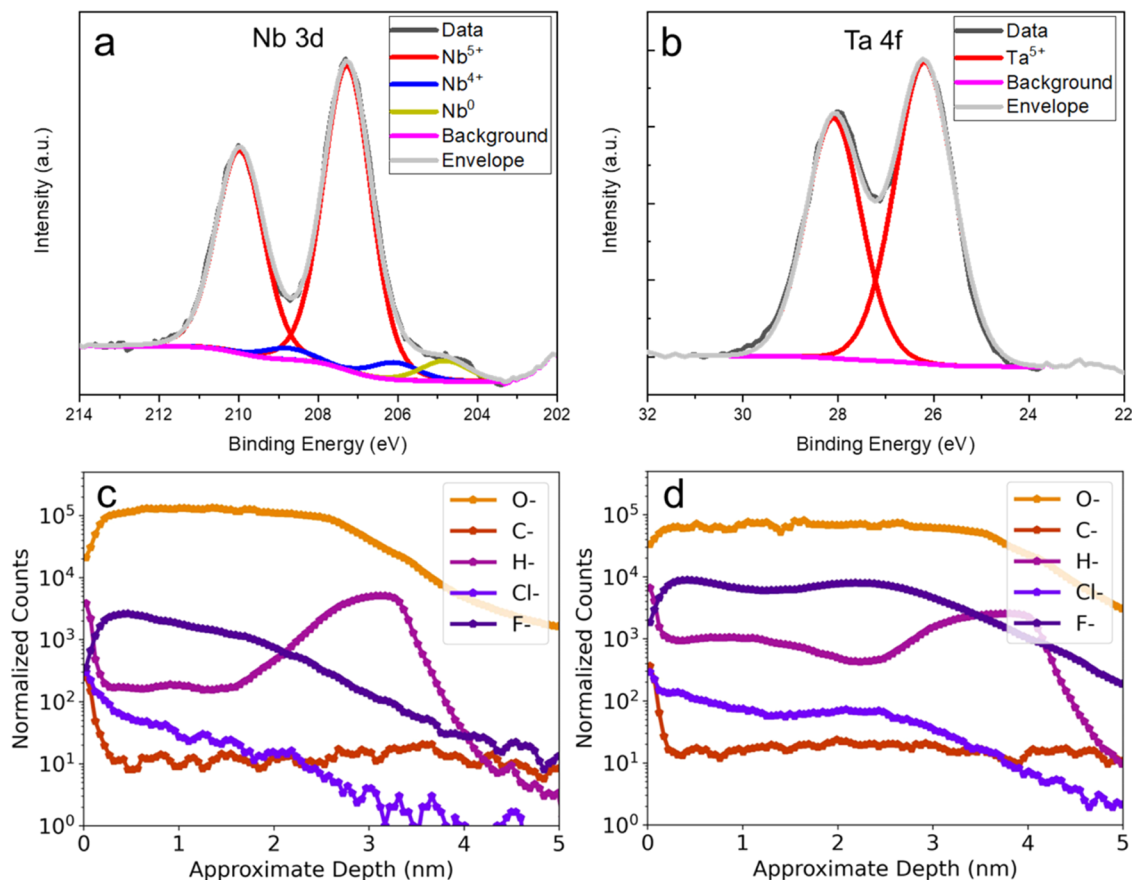


**Figure 4.** XPS and ToF-SIMS characterization. **a**, Nb 3d intensity consists of  $\text{Nb}_2\text{O}_5$ ,  $\text{NbO}_2$ , and Nb (only Nb(0) 3d 3/2 is shown). **b**, Ta 4f intensity only consists of  $\text{Ta}_2\text{O}_5$ . Black, violet, and gray lines represent the raw spectrum, background, and envelope, respectively. Normalized ToF-SIMS depth profiles showing O<sup>-</sup>, C<sup>-</sup>, H<sup>-</sup>, Cl<sup>-</sup>, and F<sup>-</sup> of **c**, bare Nb, and **d**, Ta-capped Nb thin films.

columnar grain structures, with the Nb thin films measuring approximately 200 nm thick and the Ta capping layers at around 10 nm. Notably, there is a thickness difference in the amorphous surface oxide layer between the two samples. The native amorphous surface oxide layer on the uncapped Nb film is approximately 4 nm. In comparison, the surface oxide layer on the Ta capping layer is approximately 5.5 nm (Figure 2b,g). In addition, the Ta-capped film's surface appears to follow the uncapped film's surface morphology, which aligns with the AFM analysis in Figure 1. Energy-dispersive X-ray spectroscopy (EDS) elemental distribution maps highlight these features, as depicted in Figure 2c–e,h–j. Atomic-resolution high-angle annular dark-field (HAADF)-scanning TEM (STEM) micrograph confirms the epitaxial growth of Ta on Nb due to its almost identical lattice constant, as shown in Figure 2k. The grain boundary of the Ta capping layer follows that of the Nb film, as indicated by a yellow dashed line in Figure 2k, which indicates that the Ta capping layer exhibits the same lateral grain size as the Nb thin film.

We further compared the oxygen states of Nb and Ta across the M-A interface. Figure 3 shows spatially resolved electron energy loss spectroscopy (EELS) results to elucidate the chemistry of the amorphous oxide layer. A gradual oxidation state transition is observed across the M-A interface for the amorphous Nb oxide layer. Cross-sectional HAADF-STEM images at the M-A interface indicate the spot position for spatially resolved EELS, where the distance between adjacent spots is 0.83 nm. Figure 3b displays the energy-loss near-edge

structure (ELNES) of the Nb  $M_{23}$  edge, confirming a transition from +5 to +0, indicated by two dashed lines at 365 and 363 eV, respectively. According to the Nb  $M_{23}$  edge,<sup>30</sup> the outermost four spots (1–4) correspond to the  $\text{Nb}_2\text{O}_5$ , followed by  $\text{NbO}_2$  at spot 5. This gradual transition in the oxidation state is further supported by ELNES of the O K edge (Figure 3c), where the first two dominant peaks (indicated by dashed lines at 532.5 and 535.5 eV) with a third peak at 545 eV represent higher oxidation states (+4 and +5).<sup>30</sup> The intensity ratio of the first two peaks changes slightly at spot 5, indicating a decrease in oxidation state to +4, i.e.,  $\text{NbO}_2$ .<sup>30</sup> This is consistent with our previous study<sup>31</sup> and reveals a gradual transition in the amorphous oxide layer from  $\text{Nb}_2\text{O}_5$  to  $\text{NbO}_2$  and finally  $\text{NbO}$  (spot 6) at the interface between the amorphous surface oxide layer and Nb metal.

In contrast, the Ta surface exhibits a relatively abrupt transition from  $\text{Ta}_2\text{O}_5$  to Ta. Unlike Nb, Ta lacks a core-loss edges fingerprint to track the oxidation states. However, the plasmon peaks in the low-loss energy region show an abrupt transition from spot 7 to spot 8 (Figure 3e), where spots 8 and 9 exhibit sharp plasmon peaks corresponding to metallic Ta, and spots 1 to 7 show bell-shaped plasmon peaks. The O K edge further confirms this abrupt transition, with two well-separated dominant peaks at 533.5 and 537 eV, denoted by dashed lines in Figure 3f, indicating  $\text{Ta}_2\text{O}_5$  for spots 1 to 7.<sup>32,33</sup> Therefore, based on the ELNES study across the Ta oxide layer, spot 8 may correspond to either suboxide species or a mixture of metallic Ta and some  $\text{Ta}_2\text{O}_5$ . To corroborate this,

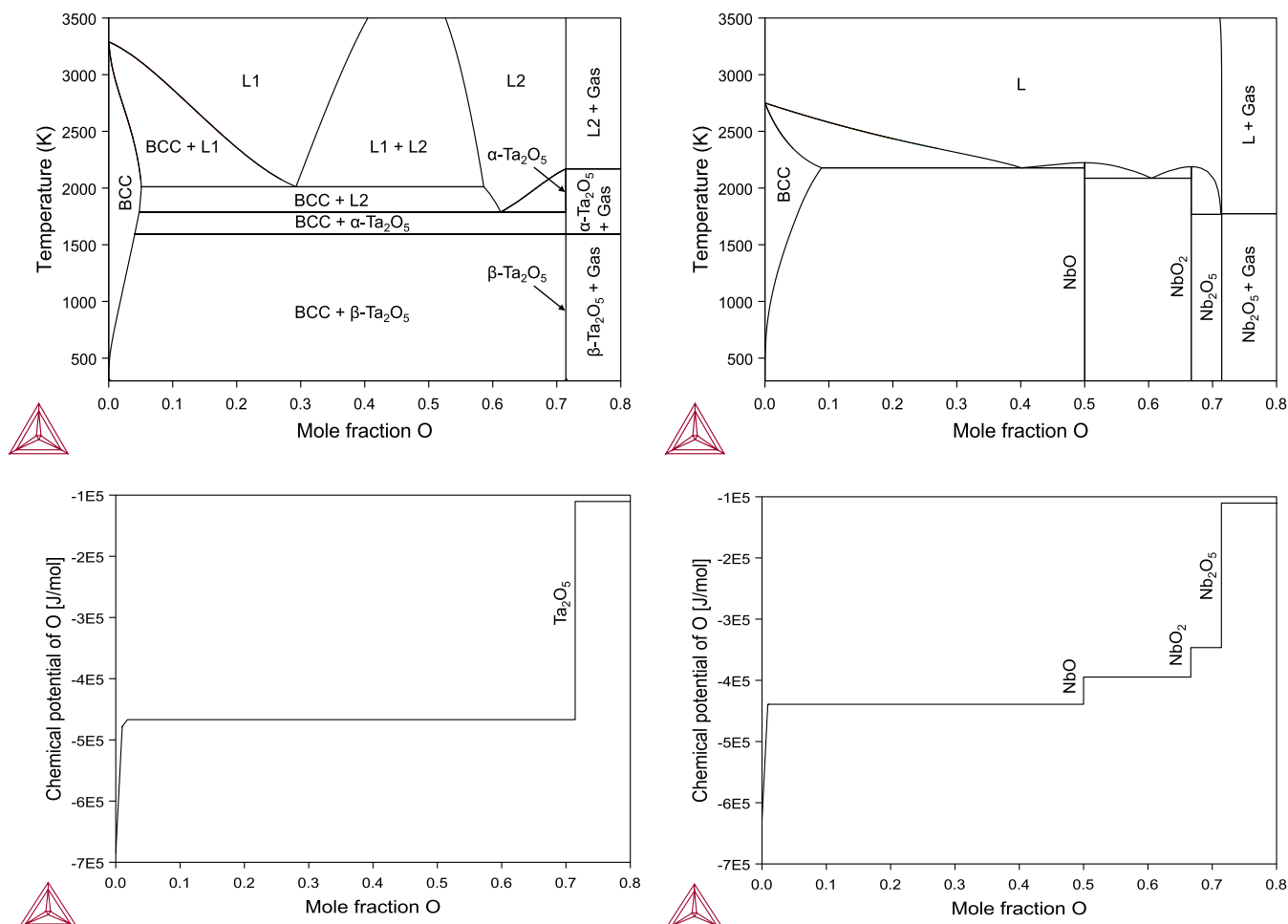


**Figure 5.** Calculated phase diagrams of the Ta–O and Nb–O systems and their respective oxygen chemical potentials as functions of oxygen mole fraction.

we performed principal component analysis (PCA). However, the PCA result did not show clear evidence of suboxide species at the Ta-TaO<sub>x</sub> interface (details in the *Supporting Information*). In general, it is evident that Ta exhibits a thinner transition layer with an upper limit of 0.8 nm and undergoes a more abrupt transition from +5 to +0 states compared to Nb (within about 0.8–1.6 nm). This observation holds true, whether conservatively or radically determined, despite the total thickness of the amorphous Ta surface oxide layer being greater than its Nb counterpart, aligning well with previous works.<sup>23,25,26</sup>

The X-ray photoelectron spectroscopy (XPS) analysis is in good agreement with the EELS results. Figure 4a shows NbO<sub>2</sub> and metallic Nb, although most of the Nb 3d intensity is Nb<sub>2</sub>O<sub>5</sub>. We do not observe a signal attributable to the NbO peak, maybe due to the small volume fraction. On the other hand, Figure 4b shows that Ta 4f is entirely explained by Ta<sub>2</sub>O<sub>5</sub> peak fits. The difference in oxide thickness may be the main reason why there are no peaks from metallic Ta, as well as Ta having a much higher atomic number that results in a shorter mean free path of electrons. It might imply that even if there are some suboxides, photoelectrons cannot escape to be detected due to the thicker Ta oxide layer. Nonetheless, with the same X-ray interaction conditions for the Nb and Ta surface oxides, the Ta-capped sample shows uniform surface oxide in the form of Ta<sub>2</sub>O<sub>5</sub>. In contrast, the baseline Nb sample

exhibits a suboxide layer between predominant Nb<sub>2</sub>O<sub>5</sub> and metallic Nb thin film, consistent with spatially resolved ELNES results in Figure 3.

To examine the impurity content in the two surface oxides, we used time-of-flight secondary ion mass spectrometry (ToF-SIMS) to capture the signal associated with species such as C<sup>-</sup>, H<sup>-</sup>, F<sup>-</sup>, and Cl<sup>-</sup> as a function of depth for both the uncapped and Ta-capped Nb films, as shown in Figure 4c,d. Regarding H<sup>-</sup> counts, we observe a clear increase in the signal close to the oxide and metal interface for both samples. As previously reported,<sup>34,35</sup> this may arise due to the infiltration of hydrogen atoms into the niobium metal before the formation of the surface oxide or during nanofabrication processes such as wet etching. Interestingly, the H<sup>-</sup> counts are found to be an order of magnitude higher in the uncapped film compared with that in the Ta-capped film.

On the other hand, the F<sup>-</sup> counts in the Ta oxide are almost an order of magnitude larger than those in the Nb oxide. The observed disparity in F<sup>-</sup> counts may explain why, in this case, we observe that Ta oxide is roughly 5 nm, whereas previous reports have indicated values closer to 3 nm.<sup>23,26,27,31,36–38</sup> While it has been reported that the tunneling of H<sup>-</sup> ions has been proposed as a loss mechanism in the GHz range,<sup>39,40</sup> it is worth noting that the F<sup>-</sup> ions are significantly larger than H<sup>-</sup> ions, and their impact on loss requires further investigation.

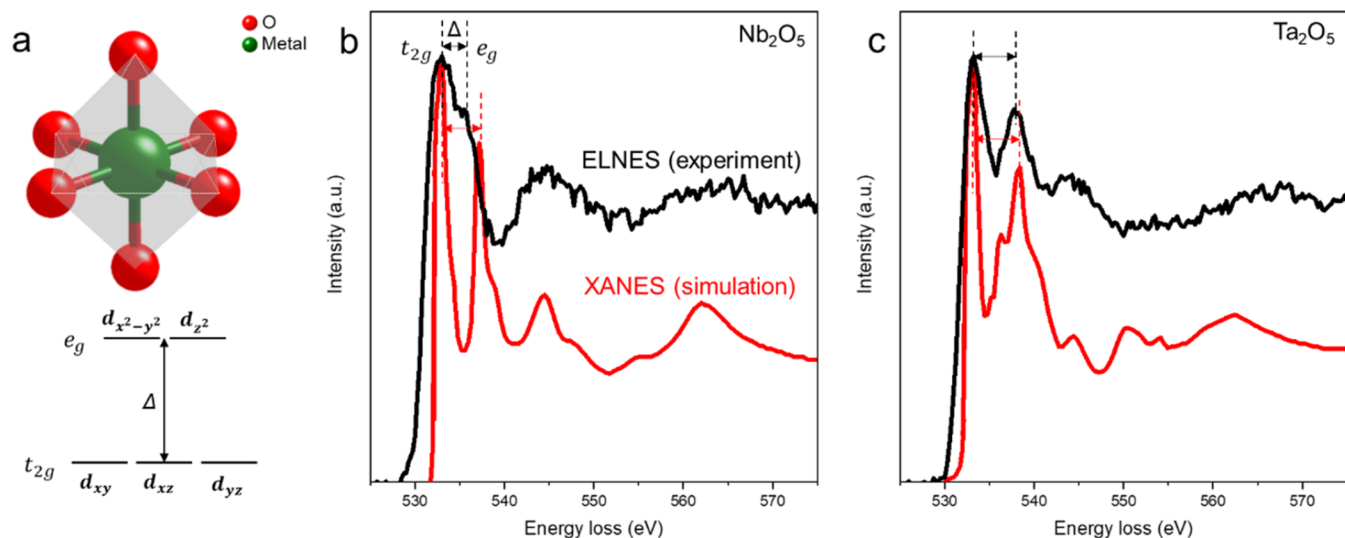


**Figure 6.** ELNES of O K edge for  $\text{Nb}_2\text{O}_5$  and  $\text{Ta}_2\text{O}_5$ . **a**, Schematic of the octahedrally coordinated transition metal ion, causing a splitting  $\Delta$  in the energy levels of the  $d$ -orbitals. **b**, O K edges of integrated experimental ELNES of amorphous  $\text{Nb}_2\text{O}_5$  and simulated XANES of crystalline  $\text{Nb}_2\text{O}_5$ . **c**, O K edges of integrated experimental ELNES of amorphous  $\text{Ta}_2\text{O}_5$  and simulated XANES of crystalline  $\text{Ta}_2\text{O}_5$ .

The experimentally observed abrupt transition in oxidation states from  $\text{Ta}_2\text{O}_5$  to Ta in contrast to the gradual shift from  $\text{Nb}_2\text{O}_5$  to Nb is consistent with the known thermodynamics. Thermodynamic descriptions of the Ta–O and Nb–O systems were obtained using the CALculation of PHase Diagrams (CALPHAD) method based on existing databases, and the resulting phase diagrams are shown in Figure 5.<sup>41–44</sup> The former has a single stable stoichiometric oxide ( $\text{Ta}_2\text{O}_5$ ), while the latter includes three oxides ( $\text{Nb}_2\text{O}_5$ ,  $\text{NbO}_2$ , and  $\text{NbO}$ ). The existence of a single valence state in the Ta–O system and three valence states in the Nb–O system is explained by the oxygen chemical potentials ( $\mu_{\text{O}}$ ) in both systems, which are plotted as functions of the oxygen mole fraction in Figure 5. There is a single discontinuity in  $\mu_{\text{O}}$  in the Ta–O system, corresponding to an abrupt change in the oxidation state. However, in the Nb–O system, three discontinuities exist in  $\mu_{\text{O}}$ , resulting in a gradual change in the oxidation state. Although the thermodynamic analysis here is based on equilibrium crystalline phases from the phase diagrams, the same trend still holds for the amorphous native oxides.

Since suboxide species may act as magnetic impurities and lead to quasiparticle loss,<sup>27,38,45,46</sup> understanding the underlying origin of enhanced performance in Ta-based qubits is often solely attributed to suboxide species. However, given that the predominant oxide species for both Nb and Ta exist in the form of their pentoxides, and extensive research indicates that  $\text{Nb}_2\text{O}_5$  is primarily accountable for two-level system (TLS) loss,<sup>17,28,29</sup> it suggests there might be another mechanism rooted in the intrinsic material properties of amorphous  $\text{Nb}_2\text{O}_5$  and  $\text{Ta}_2\text{O}_5$ . This mechanism could also play a crucial role in the performance improvement of Ta-based or Ta-capped qubits.

The unoccupied p-type states of the surrounding oxygen atoms are hybridized with the neighboring transition metal; the O K edge could provide information that reflects the bonding states in transition metal and O bonding and their oxidation states.<sup>47,48</sup> Figure 6 directly compares the ELNES of the O K edges for  $\text{Nb}_2\text{O}_5$  and  $\text{Ta}_2\text{O}_5$ . Figure 6a illustrates an octahedrally coordinated transition metal atom to oxygen

atoms, offering a qualitative explanation for the differences in the double-peak structure of the O K ELNES based on ligand-field theory. This structure results in the splitting of transition metal  $d$  orbitals into the upper,  $e_g$  orbital, and the slightly lower in energy  $t_{2g}$  with a crystal-field splitting energy  $\Delta$ .<sup>49,50</sup> Figure 6b,c presents the O K edges of measured EELS and calculated X-ray absorption spectroscopy (XAS) for  $\text{Nb}_2\text{O}_5$  and  $\text{Ta}_2\text{O}_5$ . Calculated XAS for the crystalline references is employed as EELS, essentially equivalent to XAS under high primary energy and low scattering angle approximations.<sup>47</sup> Figure 6b depicts the amorphous character of  $\text{Nb}_2\text{O}_5$ . We observe a decrease in crystal-field splitting energy  $\Delta$  compared with the crystalline counterpart and broader individual peaks. The simulated X-ray absorption near-edge structure (XANES) exhibits an  $\Delta$  of 4.15 eV, whereas experimental ELNES exhibits an  $\Delta$  of 2.5 eV, which is about a 40% reduction. This aligns with measured and calculated EELS and XAS in the literature for amorphous  $\text{Nb}_2\text{O}_5$ .<sup>48,50</sup>

In comparison, Figure 6c reveals that the crystal-field splitting energy  $\Delta$  of the measured ELNES and the calculated XAS of  $\text{Ta}_2\text{O}_5$  are almost identical (XANES with  $\Delta$  of 5.0 eV and ELNES with  $\Delta$  of 4.75 eV, which is about a 5% reduction), consistent with experimental and simulated EELS data reported in ref 33. Moreover, the measured double peaks of  $\text{Ta}_2\text{O}_5$  are sharper than those of  $\text{Nb}_2\text{O}_5$ , indicating that amorphous  $\text{Ta}_2\text{O}_5$  retains a more octahedrally symmetric crystalline character.<sup>48</sup> This implies a reduced likelihood of tunneling between the two lowest-energy states as predicted in disordered materials, resulting in fewer TLS defects being coupled with the qubit's electric field and reduced microwave loss.<sup>9,51</sup> On the other hand, amorphous  $\text{Nb}_2\text{O}_5$ , based on the measured ELNES, may have more distorted octahedrons. This distortion could lead to a higher possibility of easier tunneling between two minimum energy states, akin to the unique two-state nature of the transformation known as the umbrella flip.<sup>52</sup> As deviations from crystalline order can lead to quantum decoherence, such a phenomenon may further limit qubits' coherence time. More generally, TLS-type loss typically arises from local disorder; hence, an amorphous region is more likely to host such loss mechanisms than its crystalline counterparts.

Finally, the less distorted  $Ta_2O_5$  structure may be more effective in blocking the diffusion of H atoms toward the oxide/metal interface (Figure 4c,d), potentially further reducing TLS sources.

## CONCLUSIONS

Structural and chemical investigations were conducted on the M-A interface to elucidate the reasons behind coherence time improvement when native  $TaO_x$  was utilized instead of native  $NbO_x$ . Our observation revealed an abrupt transition from  $Ta_2O_5$  to Ta metal, marked by a significant absence of suboxide species, contrasting with the gradual valence state transition from  $Nb_2O_5$  to Nb metal in native  $NbO_x$ . The calculated phase diagram and oxygen chemical potential between Nb–O and Ta–O systems explain this disparity. In addition, we discovered a closer crystalline bonding nature of amorphous  $Ta_2O_5$  than that of  $Nb_2O_5$ . We attribute this distinction to another potential origin for the enhanced  $T_1$  of Ta or Ta-capped Nb superconducting qubits. Our comprehensive approach, combining STEM-EELS and thermodynamic calculations, elucidates the formation mechanism and low-loss nature of  $TaO_x$  compared to those of  $NbO_x$ . This insight addresses current gaps in understanding low-loss  $TaO_x$  properties, creating a foundation for subsequent in-depth theoretical investigations to validate these findings further.

## METHODS

**Qubit Fabrication.** The qubit devices were fabricated on high-resistivity Si substrates ( $\rho \geq 10 \text{ k}\Omega\cdot\text{cm}$ ) with sputter-deposited Nb (~200 nm thick) or Ta-capped (~10 nm) Nb layers and Al/ $AlO_x$ /Al Josephson junctions. Details on the thin film and device fabrication have been reported elsewhere.<sup>23</sup>

**AFM Analysis.** The surface morphology of the Nb- and Ta-capped Nb films was analyzed by AFM using an Asylum Cypher AFM with a Si cantilever in tapping mode at a scanning rate of 1 Hz. The image resolution was  $512 \times 512$  pixels.

**(S)TEM-EELS Analysis.** Cross-sectional TEM samples were prepared by using a focused ion beam instrument with a gas injection system (Helios, Thermo Fisher Scientific Ltd.). The TEM samples were thinned to electron beam transparency by a  $Ga^+$  ion beam from 30 to 2 kV. The TEM samples were investigated using an aberration-corrected TEM (Titan Cube, Thermo Fisher Scientific Ltd.) at 200 kV. A high-angle annular dark-field (HAADF) detector was used for dark-field imaging in STEM mode with a convergent semiangle and a collection semiangle of 18 and 74–200 mrad, respectively. Energy-dispersive X-ray spectroscopy (EDS) and electron energy-loss spectroscopy (EELS) studies were carried out with probe currents of 200 and 50 pA, respectively. Dual EELS was performed to acquire all-electron energy-loss (ELL) spectra. The plural scattering effect of all of the raw ELL spectra was removed via Fourier-ratio deconvolution.

**XPS Analysis.** XPS analysis was conducted with a Kratos Amicus/ESCA 3400 device, utilizing 240 W Mg  $K\alpha$  X-rays from a twin-anode laboratory source. The emitted photoelectrons were collected at a perpendicular angle to the surface and analyzed using a DuPont-type analyzer, with the pass energy adjusted to 150 eV. To refine the spectra, a Shirley baseline correction was applied using the CasaXPS software, and charging effects were compensated by calibrating the C 1s peak binding energy to 285 eV.

**ToF-SIMS Analysis.** ToF-SIMS measurements were performed using a dual beam IONTOF 5 system to analyze impurities' concentration and depth distribution in the Nb and Ta/Nb films. Secondary ion measurements were performed by using a liquid bismuth ion beam ( $Bi^+$ ). A cesium ion gun with an energy of 500 eV sputtered the surface for depth profile measurements. All counts were

normalized to the total counts in the Nb metal layer, enabling qualitative comparison of impurities between samples.

**XAS Simulation.** Simulation of X-ray absorption spectra was created by Materials Project,<sup>53</sup> for orthorhombic  $Nb_2O_5$ <sup>54</sup> and monoclinic  $Ta_2O_5$ .<sup>55</sup>

**Thermodynamic Calculations.** Thermodynamic models of the Ta–O and Nb–O systems using the CALPHAD method were adopted from a prior study<sup>41</sup> and from the TCOX11 database<sup>44</sup> in the Thermo-Calc software.<sup>43</sup> The Ta–O models include low-temperature orthorhombic ( $\beta$ ) and high-temperature tetragonal ( $\alpha$ )  $Ta_2O_5$  polymorphs, body-centered cubic (BCC)  $\alpha$ -Ta, liquid, and gas phases, which were respectively described as stoichiometric compounds, a solid solution, ionic liquid,<sup>56</sup> and ideal gas. The Nb–O models, based on unpublished work by Dupin and Ansara<sup>57</sup> and published by Massih and Pérez,<sup>58</sup> include monoclinic  $Nb_2O_5$ , tetragonal  $NbO_2$ , cubic  $NbO$ , BCC Nb, liquid, and gas phases. The compounds were modeled as stoichiometric, BCC Nb as a solid solution, the liquid as an ionic liquid, and the gas as ideal.

## ASSOCIATED CONTENT

### SI Supporting Information

The Supporting Information is available free of charge at <https://pubs.acs.org/doi/10.1021/acsnano.4c05251>.

Principal component analysis (PCA) of O K edge EELS spectra across the  $TaO_x$ -Ta interface (PDF)

## AUTHOR INFORMATION

### Corresponding Author

Lin Zhou – Ames National Laboratory, Ames, Iowa 50011, United States; Department of Materials Science and Engineering, Iowa State University, Ames, Iowa 50011, United States; [orcid.org/0000-0003-2286-6510](https://orcid.org/0000-0003-2286-6510); Email: [linzhou@ameslab.gov](mailto:linzhou@ameslab.gov)

### Authors

Jin-Su Oh – Ames National Laboratory, Ames, Iowa 50011, United States; [orcid.org/0000-0002-7462-3142](https://orcid.org/0000-0002-7462-3142)

Rahim Zaman – Department of Materials Science and Engineering, University of Virginia, Charlottesville, Virginia 22904, United States

Akshay A. Murthy – Superconducting Quantum Materials and Systems Division, Fermi National Accelerator Laboratory, Batavia, Illinois 60510, United States; [orcid.org/0000-0001-7677-6866](https://orcid.org/0000-0001-7677-6866)

Mustafa Bal – Superconducting Quantum Materials and Systems Division, Fermi National Accelerator Laboratory, Batavia, Illinois 60510, United States

Francesco Crisa – Superconducting Quantum Materials and Systems Division, Fermi National Accelerator Laboratory, Batavia, Illinois 60510, United States

Shaojiang Zhu – Superconducting Quantum Materials and Systems Division, Fermi National Accelerator Laboratory, Batavia, Illinois 60510, United States

Carlos G. Torres-Castanedo – Department of Materials Science and Engineering, Northwestern University, Evanston, Illinois 60208, United States; [orcid.org/0000-0002-4505-7970](https://orcid.org/0000-0002-4505-7970)

Cameron J. Kopas – Rigetti Computing, Berkeley, California 94710, United States

Joshua Y. Mutus – Rigetti Computing, Berkeley, California 94710, United States

Dapeng Jing – The Materials Analysis Research Laboratory, Iowa State University, Ames, Iowa 50011, United States; [orcid.org/0000-0001-7600-7071](https://orcid.org/0000-0001-7600-7071)

John Zasadzinski – Department of Physics, Illinois Institute of Technology, Chicago, Illinois 60616, United States  
Anna Grassellino – Superconducting Quantum Materials and Systems Division, Fermi National Accelerator Laboratory, Batavia, Illinois 60510, United States  
Alex Romanenko – Superconducting Quantum Materials and Systems Division, Fermi National Accelerator Laboratory, Batavia, Illinois 60510, United States  
Mark C. Hersam – Department of Materials Science and Engineering, Northwestern University, Evanston, Illinois 60208, United States;  orcid.org/0000-0003-4120-1426  
Michael J. Bedzyk – Department of Materials Science and Engineering, Northwestern University, Evanston, Illinois 60208, United States;  orcid.org/0000-0002-1026-4558  
Matt Kramer – Ames National Laboratory, Ames, Iowa 50011, United States;  orcid.org/0000-0002-9097-6730  
Bi-Cheng Zhou – Department of Materials Science and Engineering, University of Virginia, Charlottesville, Virginia 22904, United States

Complete contact information is available at:  
<https://pubs.acs.org/10.1021/acsnano.4c05251>

## Notes

The authors declare no competing financial interest. This work was produced by Iowa State University under Contract DE-AC02CH11358 with the U.S. Department of Energy. Publisher acknowledges the U.S. Government license and the provision to provide public access under the DOE Public Access Plan (<http://energy.gov/downloads/doe-public-access-plan>).

## ACKNOWLEDGMENTS

This work was supported by the U.S. Department of Energy, Office of Science, National Quantum Information Science Research Centers, Superconducting Quantum Materials and Systems Center (SQMS) under contract No. DE-AC02-07CH11359. All electron microscopy and related work were performed using instruments in the Sensitive Instrument Facility at Ames National Lab. The Ames National Laboratory is operated for the U.S. Department of Energy by Iowa State University under Contract No. DE-AC02-07CH11358. R.Z. and B.-C.Z. acknowledge Research Computing at the University of Virginia for providing computational resources and technical support that have contributed to the results reported within this manuscript. URL: <https://re.virginia.edu>. The authors also thank Rigetti Computing for fabricating the devices used in this study.

## REFERENCES

- (1) Arute, F.; Arya, K.; Babbush, R.; Bacon, D.; Bardin, J. C.; Barends, R.; Biswas, R.; Boixo, S.; Brandao, F. G. S. L.; Buell, D. A.; Burkett, B.; Chen, Y.; Chen, Z.; Chiaro, B.; Collins, R.; Courtney, W.; Dunsworth, A.; Farhi, E.; Foxen, B.; Fowler, A.; Gidney, C.; Giustina, M.; Graff, R.; Guerin, K.; Habegger, S.; Harrigan, M. P.; Hartmann, M. J.; Ho, A.; Hoffmann, M.; Huang, T.; Humble, T. S.; Isakov, S. V.; Jeffrey, E.; Jiang, Z.; Kafri, D.; Kechedzhi, K.; Kelly, J.; Klimov, P. V.; Knysh, S.; Korotkov, A.; Kostritsa, F.; Landhuis, D.; Lindmark, M.; Lucero, E.; Lyakh, D.; Mandrà, S.; McClean, J. R.; McEwen, M.; Megrant, A.; Mi, X.; Michelsen, K.; Mohseni, M.; Mutus, J.; Naaman, O.; Neeley, M.; Neill, C.; Niu, M. Y.; Ostby, E.; Petukhov, A.; Platt, J. C.; Quintana, C.; Rieffel, E. G.; Roushan, P.; Rubin, N. C.; Sank, D.; Satzinger, K. J.; Smelyanskiy, V.; Sung, K. J.; Trevithick, M. D.; Vainsencher, A.; Villalonga, B.; White, T.; Yao, Z. J.; Yeh, P.; Zalcman, A.; Neven, H.; Martinis, J. M. Quantum Supremacy Using a

- Programmable Superconducting Processor. *Nature* **2019**, *574*, 505–510.
- (2) Kim, Y.; Eddins, A.; Anand, S.; Wei, K. X.; Berg, E. van den.; Rosenblatt, S.; Nayfeh, H.; Wu, Y.; Zaletel, M.; Temme, K.; Kandala, A. Evidence for the Utility of Quantum Computing before Fault Tolerance. *Nature* **2023**, *618* (7965), 500–505.
- (3) McArdle, S.; Endo, S.; Aspuru-Guzik, A.; Benjamin, S. C.; Yuan, X. Quantum Computational Chemistry. *Rev. Mod. Phys.* **2020**, *92*, No. 15003, DOI: [10.1103/RevModPhys.92.015003](https://doi.org/10.1103/RevModPhys.92.015003).
- (4) Alam, M. S.; Belomestnykh, S.; Bornman, N.; Cancelo, G.; Chao, Y.-C.; Checchin, M.; Dinh, V. S.; Grassellino, A.; Gustafson, E. J.; Harnik, R.; McRae, C. R. H.; Huang, Z.; Kapoor, K.; Kim, T.; Kowalkowski, J. B.; Kramer, M. J.; Krasnikova, Y.; Kumar, P.; Kurkcuoglu, D. M.; Lamm, H.; Lyon, A. L.; Milathianaki, D.; Murthy, A.; Mutus, J.; Nekrashevich, I.; Oh, J.; Özgüler, A. B.; Perdue, G. N.; Reagor, M.; Romanenko, A.; Sauls, J. A.; Stefanazzi, L.; Venturelli, D.; Wang, C.; You, X.; Zanten, D. M. T. van.; Zhou, L.; Zhu, S.; Zorzetti, S. Quantum Computing Hardware for HEP Algorithms and Sensing. 2022, arXiv:2204.08605, pp 1–23. DOI: [10.48550/arXiv.2204.08605](https://doi.org/10.48550/arXiv.2204.08605).
- (5) Nielsen, M. A.; Chuang, I. L. *Quantum Computation and Quantum Information*, 10th Anniversary ed.; Cambridge University Press, 2010; p 708.
- (6) Clarke, J.; Wilhelm, F. K. Superconducting Quantum Bits. *Nature* **2008**, *453*, 1031–1042.
- (7) Kjaergaard, M.; Schwartz, M. E.; Braumüller, J.; Krantz, P.; Wang, J. I. J.; Gustavsson, S.; Oliver, W. D. Superconducting Qubits: Current State of Play. *Annu. Rev. Condens. Matter Phys.* **2020**, *11*, 369–395, DOI: [10.1146/annurev-conmatphys-031119-050605](https://doi.org/10.1146/annurev-conmatphys-031119-050605).
- (8) Lozano, D. P.; Mongillo, M.; Piao, X.; Couet, S.; Wan, D.; Canvel, Y.; Vadhiraj, A. M.; Ivanov, T.; Verjauw, J.; Acharya, R.; Damme, J. V.; Mohiyaddin, F. A.; Jussot, J.; Gowda, P. P.; Pacco, A.; Raes, B.; de Vondel, J. V.; Radu, I. P.; Govoreanu, B.; Swerts, J.; Potočnik, A.; Greve, K. D. Low-loss  $\alpha$ -tantalum coplanar waveguide resonators on silicon wafers: fabrication, characterization and surface modification. *Mater. Quantum Technol.* **2024**, *4*, No. 025801, DOI: [10.1088/2633-4356/ad4b8c](https://doi.org/10.1088/2633-4356/ad4b8c).
- (9) de Leon, N. P.; Itoh, K. M.; Kim, D.; Mehta, K. K.; Northup, T. E.; Paik, H.; Palmer, B. S.; Samarth, N.; Sangawesin, S.; Steuerman, D. W. Materials Challenges and Opportunities for Quantum Computing Hardware. *Science* **2021**, *372*, No. eabb2823, DOI: [10.1126/science.abb2823](https://doi.org/10.1126/science.abb2823).
- (10) Gyenis, A.; Paolo, A. D.; Koch, J.; Blais, A.; Houck, A. A.; Schuster, D. I. Moving beyond the Transmon: Noise-Protected Superconducting Quantum Circuits. *PRX Quantum* **2021**, *2* (3), No. 030101.
- (11) Koch, J.; Yu, T. M.; Gambetta, J.; Houck, A. A.; Schuster, D. I.; Majer, J.; Blais, A.; Devoret, M. H.; Girvin, S. M.; Schoelkopf, R. J. Charge-Insensitive Qubit Design Derived from the Cooper Pair Box. *Phys. Rev. A* **2007**, *76*, No. 042319, DOI: [10.1103/PhysRevA.76.042319](https://doi.org/10.1103/PhysRevA.76.042319).
- (12) Paik, H.; Schuster, D. I.; Bishop, L. S.; Kirchmair, G.; Catelani, G.; Sears, A. P.; Johnson, B. R.; Reagor, M. J.; Frunzio, L.; Glazman, L. I.; Girvin, S. M.; Devoret, M. H.; Schoelkopf, R. J. Observation of High Coherence in Josephson Junction Qubits Measured in a Three-Dimensional Circuit QED Architecture. *Phys. Rev. Lett.* **2011**, *107*, No. 240501, DOI: [10.1103/PhysRevLett.107.240501](https://doi.org/10.1103/PhysRevLett.107.240501).
- (13) Schreier, J. A.; Houck, A. A.; Koch, J.; Schuster, D. I.; Johnson, B. R.; Chow, J. M.; Gambetta, J. M.; Majer, J.; Frunzio, L.; Devoret, M. H.; Girvin, S. M.; Schoelkopf, R. J. Suppressing Charge Noise Decoherence in Superconducting Charge Qubits. *Phys. Rev. B* **2008**, *77*, No. 180502(R), DOI: [10.1103/PhysRevB.77.180502](https://doi.org/10.1103/PhysRevB.77.180502).
- (14) Manucharyan, V. E.; Koch, J.; Glazman, L. I.; Devoret, M. H. Fluxonium: Single Cooper-Pair Circuit Free of Charge Offsets. *Science* **2009**, *326* (5949), 113–116.
- (15) Wang, C.; Axline, C.; Gao, Y. Y.; Brecht, T.; Chu, Y.; Frunzio, L.; Devoret, M. H.; Schoelkopf, R. J. Surface Participation and Dielectric Loss in Superconducting Qubits. *Appl. Phys. Lett.* **2015**, *107* (16), No. 162601.

- (16) Oliver, W. D.; Welander, P. B. Materials in Superconducting Quantum Bits. *MRS Bull.* **2013**, *38*, 816–825.
- (17) Verjauw, J.; Potočnik, A.; Mongillo, M.; Acharya, R.; Mohiyaddin, F.; Simion, G.; Pacco, A.; Ivanov, Ts.; Wan, D.; Vanleenhove, A.; Souriau, L.; Jussot, J.; Thiam, A.; Swerts, J.; Piao, X.; Couet, S.; Heyns, M.; Govoreanu, B.; Radu, I. Investigation of Microwave Loss Induced by Oxide Regrowth in High-Q Niobium Resonators. *Phys. Rev. Appl.* **2021**, *16* (1), No. 014018.
- (18) Murray, C. E. Material Matters in Superconducting Qubits. *Mater. Sci. Eng., R* **2021**, *146*, No. 100646, DOI: [10.1016/j.mser.2021.100646](https://doi.org/10.1016/j.mser.2021.100646).
- (19) Schoelkopf, R. J.; Girvin, S. M. Wiring up Quantum Systems. *Nature* **2008**, *451*, 664–669.
- (20) Guo, X.; Degnan, Z.; Steele, J. A.; Solano, E.; Donose, B. C.; Bertling, K.; Fedorov, A.; Rakić, A. D.; Jacobson, P. Near-Field Localization of the Boson Peak on Tantalum Films for Superconducting Quantum Devices. *J. Phys. Chem. Lett.* **2023**, *14* (20), 4892–4900.
- (21) Premkumar, A.; Weiland, C.; Hwang, S.; Jäck, B.; Place, A. P. M.; Waluyo, I.; Hunt, A.; Bisogni, V.; Pelliciari, J.; Barbour, A.; Miller, M. S.; Russo, P.; Camino, F.; Kisslinger, K.; Tong, X.; Hybertsen, M. S.; Houck, A. A.; Jarrige, I. Microscopic Relaxation Channels in Materials for Superconducting Qubits. *Commun. Mater.* **2021**, *2*, 72 DOI: [10.1038/s43246-021-00174-7](https://doi.org/10.1038/s43246-021-00174-7).
- (22) Nersisyan, A.; Sete, E. A.; Stanwyck, S.; Bestwick, A.; Reagor, M.; Poletto, S.; Alidoust, N.; Manenti, R.; Renzas, R.; Bui, C. V.; Vu, K.; Whyland, T.; Mohan, Y. Manufacturing Low Dissipation Superconducting Quantum Processors. In Technical Digest—International Electron Devices Meeting, IEDM; IEEE: San Francisco, CA, USA, 2019; pp 31.1.1–31.1.4 DOI: [10.1109/iedm19573.2019.8993458](https://doi.org/10.1109/iedm19573.2019.8993458).
- (23) Bal, M.; Murthy, A. A.; Zhu, S.; Crisa, F.; You, X.; Huang, Z.; Roy, T.; Lee, J.; Zanten, D.; van Pilipenko, R.; Nekrashevich, I.; Lunin, A.; Bafia, D.; Krasnikova, Y.; Kopas, C. J.; Lachman, E. O.; Miller, D.; Mutus, J. Y.; Reagor, M. J.; Cansizoglu, H.; Marshall, J.; Pappas, D. P.; Vu, K.; Yadavalli, K.; Oh, J.-S.; Zhou, L.; Kramer, M. J.; Lecocq, F. Q.; Goronzy, D. P.; Torres-Castanedo, C. G.; Pritchard, G.; Dravid, V. P.; Rondinelli, J. M.; Bedzyk, M. J.; Hersam, M. C.; Zasadzinski, J.; Koch, J.; Sauls, J. A.; Romanenko, A.; Grassellino, A. Systematic Improvements in Transmon Qubit Coherence Enabled by Niobium Surface Encapsulation. *npj Quantum Inf.* **2024**, *10*, No. 43, DOI: [10.1038/s41534-024-00840-x](https://doi.org/10.1038/s41534-024-00840-x).
- (24) Place, A. P. M.; Rodgers, L. V. H.; Mundada, P.; Smitham, B. M.; Fitzpatrick, M.; Leng, Z.; Premkumar, A.; Bryon, J.; Vrajitoarea, A.; Sussman, S.; Cheng, G.; Madhavan, T.; Babla, H. K.; Le, X. H.; Gang, Y.; Jäck, B.; Gyenis, A.; Yao, N.; Cava, R. J.; Leon, N. P. de.; Houck, A. A. New Material Platform for Superconducting Transmon Qubits with Coherence Times Exceeding 0.3 ms. *Nat. Commun.* **2021**, *12*, No. 1779.
- (25) Wang, C.; Li, X.; Xu, H.; Li, Z.; Wang, J.; Yang, Z.; Mi, Z.; Liang, X.; Su, T.; Yang, C.; Wang, G.; Wang, W.; Li, Y.; Chen, M.; Li, C.; Linghu, K.; Han, J.; Zhang, Y.; Feng, Y.; Song, Y.; Ma, T.; Zhang, J.; Wang, R.; Zhao, P.; Liu, W.; Xue, G.; Jin, Y.; Yu, H. Towards Practical Quantum Computers: Transmon Qubit with a Lifetime Approaching 0.5 ms. *npj Quantum Inf.* **2022**, *8*, No. 3, DOI: [10.1038/s41534-021-00510-2](https://doi.org/10.1038/s41534-021-00510-2).
- (26) McLellan, R. A.; Dutta, A.; Zhou, C.; Jia, Y.; Weiland, C.; Gui, X.; Place, A. P. M.; Crowley, K. D.; Le, X. H.; Madhavan, T.; Gang, Y.; Baker, L.; Head, A. R.; Waluyo, I.; Li, R.; Kisslinger, K.; Hunt, A.; Jarrige, I.; Lyon, S. A.; Barbour, A. M.; Cava, R. J.; Houck, A. A.; Hulbert, S. L.; Liu, M.; Walter, A. L.; Leon, N. P. de. Chemical Profiles of the Oxides on Tantalum in State of the Art Superconducting Circuits. *Adv. Sci.* **2023**, *10*, No. e2300921.
- (27) Mun, J.; Sushko, P. V.; Brass, E.; Zhou, C.; Kisslinger, K.; Qu, X.; Liu, M.; Zhu, Y. Probing Oxidation-Driven Amorphized Surfaces in a Ta(110) Film for Superconducting Qubit. *ACS Nano* **2024**, *18* (1), 1126–1136.
- (28) Romanenko, A.; Pilipenko, R.; Zorzetti, S.; Frolov, D.; Awida, M.; Belomestnykh, S.; Posen, S.; Grassellino, A. Three-Dimensional Superconducting Resonators at T < 20 MK with Photon Lifetimes up to T = 2 s. *Phys. Rev. Appl.* **2020**, *13*, No. 034032, DOI: [10.1103/PhysRevApplied.13.034032](https://doi.org/10.1103/PhysRevApplied.13.034032).
- (29) Romanenko, A.; Schuster, D. I. Understanding Quality Factor Degradation in Superconducting Niobium Cavities at Low Microwave Field Amplitudes. *Phys. Rev. Lett.* **2017**, *119*, No. 264801, DOI: [10.1103/PhysRevLett.119.264801](https://doi.org/10.1103/PhysRevLett.119.264801).
- (30) Bach, D.; Schneider, R.; Gerthsen, D.; Verbeeck, J.; Sigle, W. EELS of Niobium and Stoichiometric Niobium-Oxide Phases—Part I: Plasmon and Near-Edges Fine Structure. *Microsc. Microanal.* **2009**, *15* (6), 505–523.
- (31) Oh, J.-S.; Fang, X.; Kim, T.-H.; Lynn, M.; Kramer, M.; Zarea, M.; Sauls, J. A.; Romanenko, A.; Posen, S.; Grassellino, A.; Kopas, C. J.; Field, M.; Marshall, J.; Cansizoglu, H.; Yadavalli, K.; Mutus, J. Y.; Reagor, M.; Zhou, L. In-Situ Transmission Electron Microscopy Investigation on Surface Oxides Thermal Stability of Niobium. *Appl. Surf. Sci.* **2023**, *627*, No. 157297, DOI: [10.1016/j.apsusc.2023.157297](https://doi.org/10.1016/j.apsusc.2023.157297).
- (32) Park, G.-S.; Kim, Y. B.; Park, S. Y.; Li, X. S.; Heo, S.; Lee, M.-J.; Chang, M.; Kwon, J. H.; Kim, M.; Chung, U.-I.; Dittmann, R.; Waser, R.; Kim, K. In Situ Observation of Filamentary Conducting Channels in an Asymmetric Ta<sub>2</sub>O<sub>5</sub>-x/TaO<sub>2</sub>-x Bilayer Structure. *Nat. Commun.* **2013**, *4*, No. 2382.
- (33) Schaltin, S.; D'Urzo, L.; Zhao, Q.; Vantomme, A.; Plank, H.; Kothleitner, G.; Gspan, C.; Binnemans, K.; Fransaer, J. Direct Electroplating of Copper on Tantalum from Ionic Liquids in High Vacuum: Origin of the Tantalum Oxide Layer. *Phys. Chem. Chem. Phys.* **2012**, *14*, 13624–13629.
- (34) Lee, J.; Sung, Z.; Murthy, A. A.; Reagor, M.; Grassellino, A.; Romanenko, A. Discovery of Nb Hydride Precipitates in Superconducting Qubits. 2021, arXiv 2108.10385 DOI: [10.48550/arXiv.2108.10385](https://doi.org/10.48550/arXiv.2108.10385).
- (35) Torres-Castanedo, C. G.; Goronzy, D. P.; Pham, T.; McFadden, A.; Materise, N.; Das, P. M.; Cheng, M.; Lebedev, D.; Ribet, S. M.; Walker, M. J.; Garcia-Wetten, D. A.; Kopas, C. J.; Marshall, J.; Lachman, E.; Zhelev, N.; Sauls, J. A.; Mutus, J. Y.; McRae, C. R. H.; Dravid, V. P.; Bedzyk, M. J.; Hersam, M. C. Formation and Microwave Losses of Hydrides in Superconducting Niobium Thin Films Resulting from Fluoride Chemical Processing *Adv. Funct. Mater.* **2024** 2401365 DOI: [10.1002/adfm.202401365](https://doi.org/10.1002/adfm.202401365).
- (36) Murthy, A. A.; Lee, J.; Kopas, C.; Reagor, M. J.; McFadden, A. P.; Pappas, D. P.; Checchin, M.; Grassellino, A.; Romanenko, A. TOF-SIMS Analysis of Decoherence Sources in Superconducting Qubits. *Appl. Phys. Lett.* **2022**, *120*, No. 044002, DOI: [10.1063/5.0079321](https://doi.org/10.1063/5.0079321).
- (37) Murthy, A. A.; Das, P. M.; Ribet, S. M.; Kopas, C.; Lee, J.; Reagor, M. J.; Zhou, L.; Kramer, M. J.; Hersam, M. C.; Checchin, M.; Grassellino, A.; Reis, R. dos.; Dravid, V. P.; Romanenko, A. Developing a Chemical and Structural Understanding of the Surface Oxide in a Niobium Superconducting Qubit. *ACS Nano* **2022**, *16*, 17257–17262, DOI: [10.1021/acsnano.2c07913](https://doi.org/10.1021/acsnano.2c07913).
- (38) Altoé, M. V. P.; Banerjee, A.; Berk, C.; Hajr, A.; Schwartzberg, A.; Song, C.; Alghadeer, M.; Aloni, S.; Elowson, M. J.; Kreikebaum, J. M.; Wong, E. K.; Griffin, S. M.; Rao, S.; Weber-Bargioni, A.; Minor, A. M.; Santiago, D. I.; Cabrini, S.; Siddiqi, I.; Ogletree, D. F. Localization and Mitigation of Loss in Niobium Superconducting Circuits. *PRX Quantum* **2022**, *3*, No. 020312.
- (39) Wang, Z.; Wang, H.; Yu, C. C.; Wu, R. Q. Hydrogen as a Source of Flux Noise in SQUIDS. *Phys. Rev. B* **2018**, *98* (2), No. 020403.
- (40) Zarea, M.; Ueki, H.; Sauls, J. A. Effects of Anisotropy and Disorder on the Superconducting Properties of Niobium. *Front. Phys.* **2023**, *11*, No. 1269872.
- (41) Meisner, K. J.; Zaman, R.; Zhou, B.-C. Thermodynamic Modeling of the Ta-O System. *Calphad* **2022**, *76*, No. 102391.
- (42) Pérez, R. J.; Massih, A. R. Thermodynamic Evaluation of the Nb-O-Zr System. *J. Nucl. Mater.* **2007**, *360* (3), 242–254.
- (43) Andersson, J.-O.; Helander, T.; Höglund, L.; Shi, P.; Sundman, B. Thermo-Calc & DICTRA, Computational Tools for Materials Science. *Calphad* **2002**, *26* (2), 273–312.

- (44) Thermo-Calc. Thermo-Calc Oxide Solutions Database Version 11.1.
- (45) Proslier, T.; Kharitonov, M.; Pellin, M.; Zasadzinski, J.; Ciovati, G. Evidence of Surface Paramagnetism in Niobium and Consequences for the Superconducting Cavity Surface Impedance. *IEEE Trans. Appl. Supercond.* **2011**, *21*, 2619–2622, DOI: 10.1109/TASC.2011.2107491.
- (46) Sheridan, E.; Harrelson, T. F.; Sivonxay, E.; Persson, K. A.; Altoé, M. V. P.; Siddiqi, I.; Ogletree, D. F.; Santiago, D. I.; Griffin, S. M. Microscopic Theory of Magnetic Disorder-Induced Decoherence in Superconducting Nb Films. 2021, arXiv 2111.11684, pp 1–10 DOI: 10.48550/arXiv.2111.11684.
- (47) Frati, F.; Hunault, M. O. J. Y.; de Groot, F. M. F. Oxygen K-Edge X-Ray Absorption Spectra. *Chem. Rev.* **2020**, *120*, 4056–4110, DOI: 10.1021/acs.chemrev.9b00439.
- (48) Harrelson, T. F.; Sheridan, E.; Kennedy, E.; Vinson, J.; N'Diaye, A. T.; Altoé, M. V. P.; Schwartzberg, A.; Siddiqi, I.; Ogletree, D. F.; Scott, M. C.; Griffin, S. M. Elucidating the Local Atomic and Electronic Structure of Amorphous Oxidized Superconducting Niobium Films. *Appl. Phys. Lett.* **2021**, *119*, No. 244004.
- (49) Coulson, C. A. Transition-Metal Chemistry. *Nature* **1961**, *191* (4795), 1233–1234.
- (50) Bach, D. EELS Investigations of Stoichiometric Niobium Oxides and Niobium-Based Capacitors, PhD thesis; 2009, p 210.
- (51) Müller, C.; Cole, J. H.; Lisenfeld, J. Towards Understanding Two-Level-Systems in Amorphous Solids: Insights from Quantum Circuits. *Rep. Prog. Phys.* **2019**, *82*, No. 124501.
- (52) Kolobov, A. V.; Fons, P.; Frenkel, A. I.; Ankudinov, A. L.; Tominaga, J.; Uruga, T. Understanding the Phase-Change Mechanism of Rewritable Optical Media. *Nat. Mater.* **2004**, *3* (10), 703–708.
- (53) Jain, A.; Ong, S. P.; Hautier, G.; Chen, W.; Richards, W. D.; Dacek, S.; Cholia, S.; Gunter, D.; Skinner, D.; Ceder, G.; Persson, K. A. Commentary: The Materials Project: A Materials Genome Approach to Accelerating Materials Innovation. *APL Mater.* **2013**, *1* (1), No. 011002.
- (54) Project, T. M. Materials Data on Nb<sub>2</sub>O<sub>5</sub> by Materials Project. 2020. DOI: 10.17188/1304538.
- (55) Project, T. M. Materials Data on Ta<sub>2</sub>O<sub>5</sub> by Materials Project. 2020. DOI: 10.17188/1307209.
- (56) Hillert, M.; Jansson, B.; Sundman, B.; ågren, J. A Two-Sublattice Model for Molten Solutions with Different Tendency for Ionization. *Metall. Trans. A* **1985**, *16* (2), 261–266, DOI: 10.1007/BF02816052.
- (57) Dupin, N.; Ansara, I. Unpublished Communication with N. Dupin; 2005.
- (58) Massih, A. R.; Pérez, R. J. *Thermodynamic Evaluation of the Nb-O System*; Technical Report. 2006, PM 05–002 v2; Quantum Technologies AB: Uppsala, Sweden.

#### NOTE ADDED AFTER ASAP PUBLICATION

After this paper was published ASAP July 22, 2024, we corrected a spelling error in the name of author Carlos G. Torres Castanedo. The corrected version was reposted July 30, 2024.